Coastal freshening enhances eddy-driven heat transfer toward the Antarctic margins

Yidongfang Si[1]*, Andrew L. Stewart[1], Ian Eisenman[2]

The Antarctic Slope Front (ASF) is a strong gradient in water mass properties close to the Antarctic margins. Heat transport across the ASF is important to Earth's climate, as it influences melting of ice shelves, the formation of bottom water, and thus the global meridional overturning circulation. Previous studies based on relatively low-resolution models have reported contradictory findings regarding the impact of additional meltwater on onshore heat transport onto the Antarctic continental shelf: it remains unclear whether meltwater enhances shoreward heat transport, leading to a positive feedback, or further isolates the continental shelf from the open ocean. In this study, heat transport across the ASF is investigated using high-resolution, process-oriented simulations. It is found that shoreward heat transport is primarily controlled by the salinity gradient of the shelf waters: both freshening and salinification of the shelf waters relative to the offshore waters lead to increased heat flux onto the continental shelf. For salty shelves, the overturning consists of a dense water outflow that drives a shoreward heat flux near the seafloor; for fresh shelves, there is a shallow, eddy-driven overturning circulation that is associated with an export of fresh surface waters and a near-surface shoreward heat flux. The eddy-driven overturning associated with coastal freshening may lead to a positive feedback in a warming climate: large volumes of meltwater increase shoreward heat transport, causing further melt of ice shelves.

Recent studies have shown that the volume loss from Antarctic ice shelves is accelerating[47;48], which is largely attributed to ocean-driven basal melt[48;9;1]. Observations and model projections have indicated a widespread freshening of the Antarctic margins due to increased meltwater discharge[25;27;53;64;37;51]. Coastal freshening can reshape the ocean circulation around the Antarctic margins[19] and potentially modify the shoreward ocean heat transfer. Therefore, understanding the interplay between meltwater discharge and ocean heat transport is critical for predicting future climate change, especially sea-level rise[28], dense water formation, and the global overturning circulation[67]. Fig. 1a shows the winter climatology of ocean salinity at 500 m depth, or at the seafloor where the ocean is shallower than 500 m. In the Ross Sea and the Weddell Sea, where the Antarctic bottom water is formed, the coastal salinity is relatively high. Close to the Antarctic Peninsula and in East Antarctica, the continental shelves are fresher than the water masses offshore. Fig. 1b-c show cross sections of ocean salinity, highlighting the "fresh shelves" and "dense shelves" around Antarctica.

As a strong gradient in water mass properties between the cold shelf water and the warmer Circumpolar Deep Water (CDW), the Antarctic Slope Front (ASF) is essential in ocean heat transfer toward the Antarctic margins[67]. The ASF, and the associated westward Antarctic Slope Current (ASC), form a barrier to exchanges such as heat, freshwater, and nutrients between the continental shelf and the open ocean[26;74;21], except along the West Antarctic Peninsula[67]. The arrows in Fig. 1a indicate the major ocean current systems around the Antarctic margins, with ASC highlighted in white. In the Bellingshausen Sea and the Amundsen Sea where the ASC is weaker, denoted by the white dashed curve in Fig. 1a, warm water at depth can access ice shelves via submarine troughs[67], leading to the highest ice shelf thinning rates around Antarctica[48;9;47], and thereby to coastal freshening. Though wind and buoyancy forcing have historically been recognized as key drivers of the ASC[26;74;17], there are mounting studies that emphasize the role of small-scale and/or high-frequency variability in the cross-slope heat and water mass exchanges, such as mesoscale eddies[44;66;62;63], tides[46;41;23;11], dense outflows[73], and shelf waves[29;58].

Previous studies with relatively coarse resolution show that coastal freshening leads to increased shoreward heat transport, which triggers strong subsurface warming around Antarctica[38;12;5;52;50]. For example, Golledge et al. (2019)[15] found that meltwater from Antarctica will trap warm water below the sea surface, creating a positive feedback that increases Antarctic ice loss. Some other studies have opposite predictions of ocean heat transport in response to meltwater[2;65]. Using a global ocean-sea ice model, Moorman et al. (2020)[39] found that coastal freshening tends to isolate the continental shelves from offshore heat. However, these modeling studies with relatively coarse resolution did not fully resolve mesoscale eddies in their simulations due to the small Rossby radius of deformation[59;62], thus potentially omitted a key source of onshore ocean heat transfer contributed by eddies. Nakayama et al. (2021)[43] found increased shoreward heat transport associated with coastal freshening in East Antarctica, using a horizontal grid spacing of 3-4 km. However, the mechanism underlying the increased heat transport remains unclear.

In this study, we show that if the resolution is high enough to resolve mesoscale eddies over the continental shelf and slope, coastal freshening leads to increased shoreward heat transport. In addition, we provide insight into the dynamic mechanisms of shoreward ocean heat transport driven by eddies, tides, and mean

[1]Department of Atmospheric and Oceanic Sciences, University of California, Los Angeles, Los Angeles, CA, USA.
[2]Scripps Institution of Oceanography, University of California, San Diego, La Jolla, CA, USA.
*e-mail: csi@atmos.ucla.edu

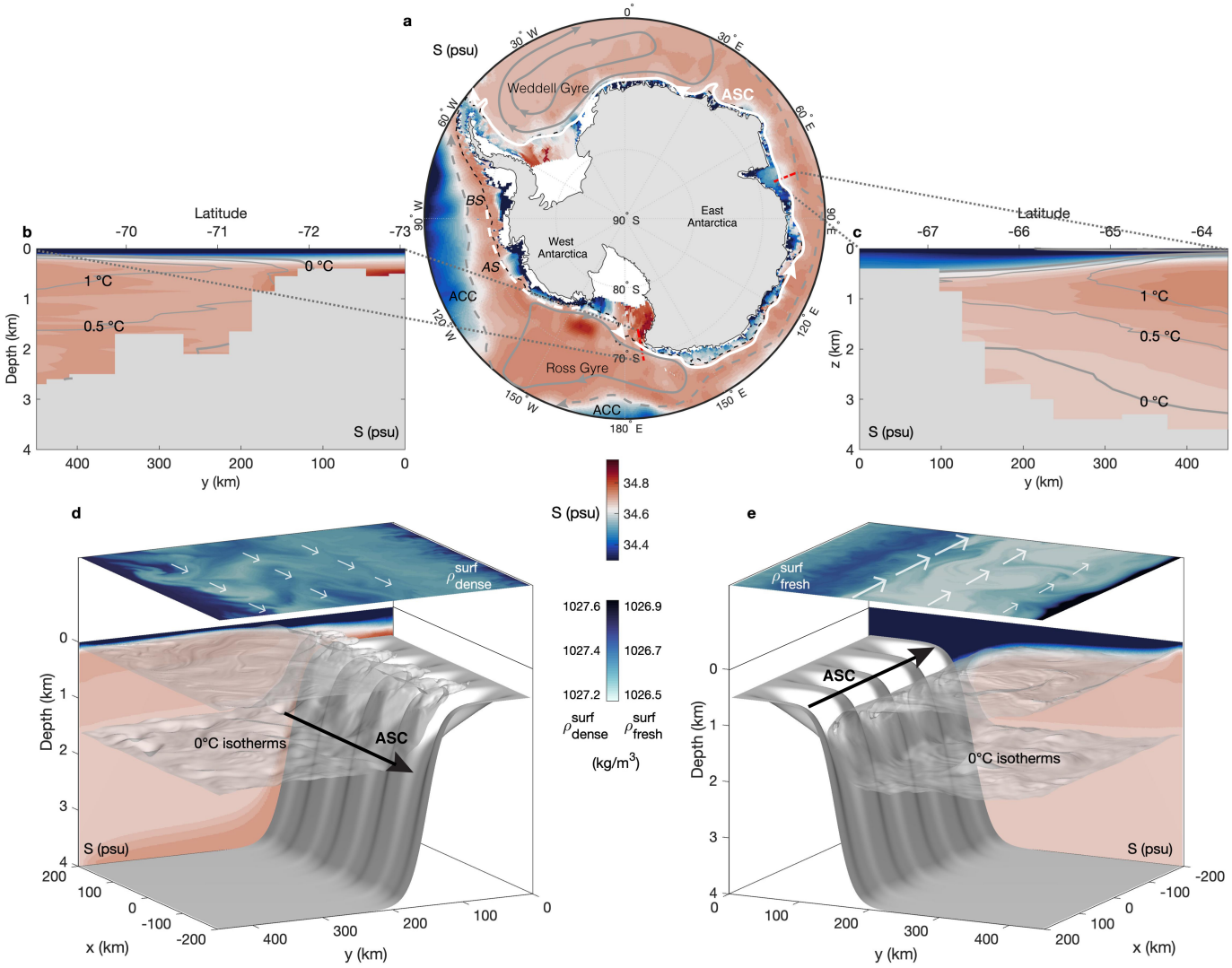

Fig. 1 | **Salinity regimes around Antarctica and in our model configuration.** **a**, winter climatology (1981-2010) of 500-m depth ocean salinity or seafloor salinity where the ocean is shallower than 500 m. The black dashed curve indicates the 1,000 m isobath. The white arrows represent the Antarctic Slope Current (ASC), with white dashed lines in the Bellingshausen (BS), Amundsen (AS), and Ross Seas denoting the uncertain initiation of the ASC[67]. The solid gray arrows represent the Ross Gyre and the Weddell Gyre. The dashed gray arrows represent the Antarctic Circumpolar Current (ACC). **b**, a cross section of ocean salinity taken in the Ross Sea (73.05°-69.01°S, 172.13°E), where the shelf is relatively salty, overlaid by gray contours of surface-referenced potential temperature. **c**, a cross section of ocean salinity taken in East Antarctica (67.75°-63.71°S, 76.38°E), where the shelf is relatively fresh, overlaid by gray contours of surface-referenced potential temperature. The data used in **a-c** comes from World Ocean Atlas 2018[77]. **d**, results of the dense-shelf (equivalent to "salty-shelf" in this study) simulation with instantaneous sea surface potential density, 0°C isotherms, and time- and zonal-mean salinity in the background. The white arrows denote the direction and relative strength of sea surface currents, and the black arrow schematically shows the direction of the ASC. **e**, similar to **d**, shows the fresh-shelf simulation. The colorbar spacing is 0.016 psu for salinity, and 0.01 kg/m^3 for surface potential density.

flows, as well as its sensitivity to wind forcing, sea ice, and topography.

Model configuration

In this study, we use a high-resolution process-oriented model developed by Si et al. (submitted)[54], based on the Massachusetts Institute of Technology General Circulation Model (MITgcm)[34;35]. We use an ocean/sea ice model because the ocean-sea ice interaction exerts an important dynamical influence on the ASF/ASC[67;54]. The model solves the hydrostatic Boussinesq equations with high-order polynomials for the equation of state[36]. The model simulates sea ice dynamics[33] using a viscous-plastic ice rheology[22] and thermodynamics with seven sea ice thickness categories[75]. We need to use high resolution to resolve mesoscale eddies over the shelf and slope[59;62], and hence we adopt a small domain (450 km by 400 km by 4 km) and fine horizontal grid spacing (2 km). The vertical grid spacing ranges from 10 m at the surface to 100 m at the bottom with 70 vertical levels. We exclude seasonal variations from our simulations, and set the atmospheric properties to minimize the net air-ice thermodynamic fluxes to preserve a relatively uniform sea ice cover, because this is

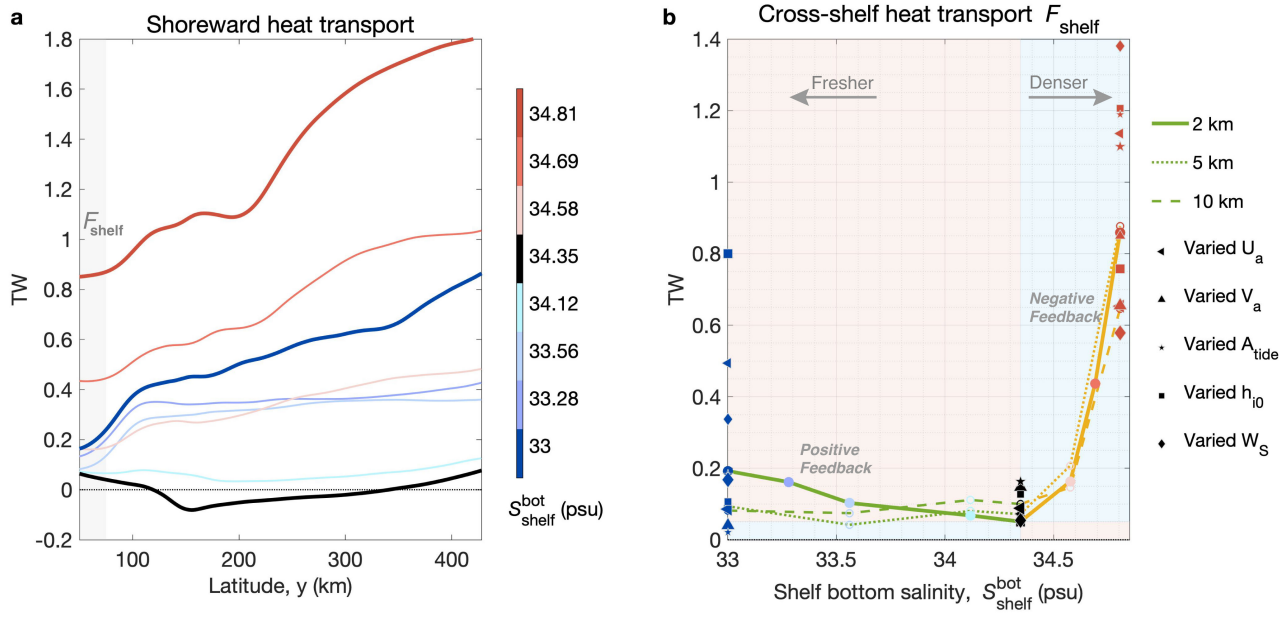

Fig. 2 | Sensitivity of shoreward heat transport. a, vertically and zonally integrated meridional advective heat flux in the simulations with varied shelf bottom salinity (S^{bot}_{shelf}) in TW (1 TW = 10^{12} W), as a function of latitude y. The horizontal resolution of these simulations is 2 km. Light gray denotes the latitudinal band (50 km–75 km) used to calculate the averaged heat transferred onto the shelf, F_{shelf}. The 20-km sponge layers in the northern and southern boundaries are excluded. **b**, heat transferred onto the continental shelf (F_{shelf}), as a function of shelf bottom salinity prescribed at the southern boundary. The solid, dotted, and dashed lines denote simulations with 2-km, 5-km, and 10-km resolution, respectively. In the background, light red denotes regions of positive feedback, and light blue denotes regions of negative feedback. For the fresh-shelf, reference, and dense-shelf cases, the sensitivities of F_{shelf} to other model parameters are marked with various shapes, with larger marker sizes corresponding to larger values of parameters.

the representative of the typical conditions in Antarctica[54]. Idealized wind forcing and tidal currents are imposed based on typical conditions observed near the Antarctic margins (see Methods). We impose the bulk meridional density gradient as a control parameter via two 20-km-wide sponge layers at the northern and southern boundaries. At the northern boundary, we restore the ocean temperature and salinity to the winter climatology of hydrography taken at East Antarctica[18]. At the southern boundary, the potential temperature is vertically uniform and equal to the freezing temperature, as typically observed[31], and we impose a linear vertical profile of salinity. We control the offshore density gradient by varying the maximum salinity and salinity gradient at the southern boundary.

Fig. 1d and 1e show the state of the ocean in the dense-shelf and fresh-shelf cases. The ASC flows westward along the slope, and shifts from a surface-intensified current in the fresh-shelf case (Fig. 1e) to a bottom-intensified current in the dense-shelf case (Fig. 1d), consistent with observations[30]. We explored the following parameters in our simulations: salinity at the southern boundary, wind speeds, tidal amplitude, sea ice thickness, and continental slope width. We additionally run simulations using coarser horizontal grid spacings (5 km and 10 km) for comparison with our high-resolution (2 km) runs. We run these coarse simulations with and without the standard Gent-McWilliams/Redi (GM-Redi) parameterization schemes for mesoscale eddies[13;14;49] to evaluate the ability of coarser-resolution models to capture the shoreward heat transfer.

Results

Fig. 2 shows the sensitivity of shoreward heat transport. We find that the shoreward heat transport is largely controlled by the magnitude of the cross-slope salinity gradient (equivalently offshore buoyancy gradient), with some other parameters such as sea ice thickness and slope width greatly enhancing shoreward heat transport in the fresh-shelf and dense-shelf cases (Fig. 2b). The shoreward heat flux is very close to zero in the reference case with no offshore buoyancy gradient. Both freshening and salinification of the shelf waters relative to the offshore waters lead to increased heat flux onto the continental shelf (Fig. 2a). The heat convergence over the continental shelf and slope is locally balanced by ocean-sea ice heat flux due to sea ice melting, which is sensitive to tidal amplitude. For continental shelves with large volumes of meltwater (fresh shelves), increased heat transport with freshening indicates further melt of the ice shelves, and thus we expect a positive feedback based on previous studies[15;38;52]. For salty shelves with dense water production, since the shoreward heat transport increases with salinification, causing further melt and leading to freshening, we expect a negative feedback in the dense-shelf regime.

The perturbation experiments show that the sensitivity of shoreward heat transport is complicated, depending on the salinity regime (Fig. 2b) and offshore distance (Extended Data Fig. 2). For the reference shelf salinity, the shoreward heat transport increases with larger tidal amplitude, stronger meridional winds, or thinner sea ice. For fresh shelves, the shoreward heat transport increases greatly with thicker sea ice, weaker zonal wind, or steeper continental slope. For dense shelves, the shoreward heat

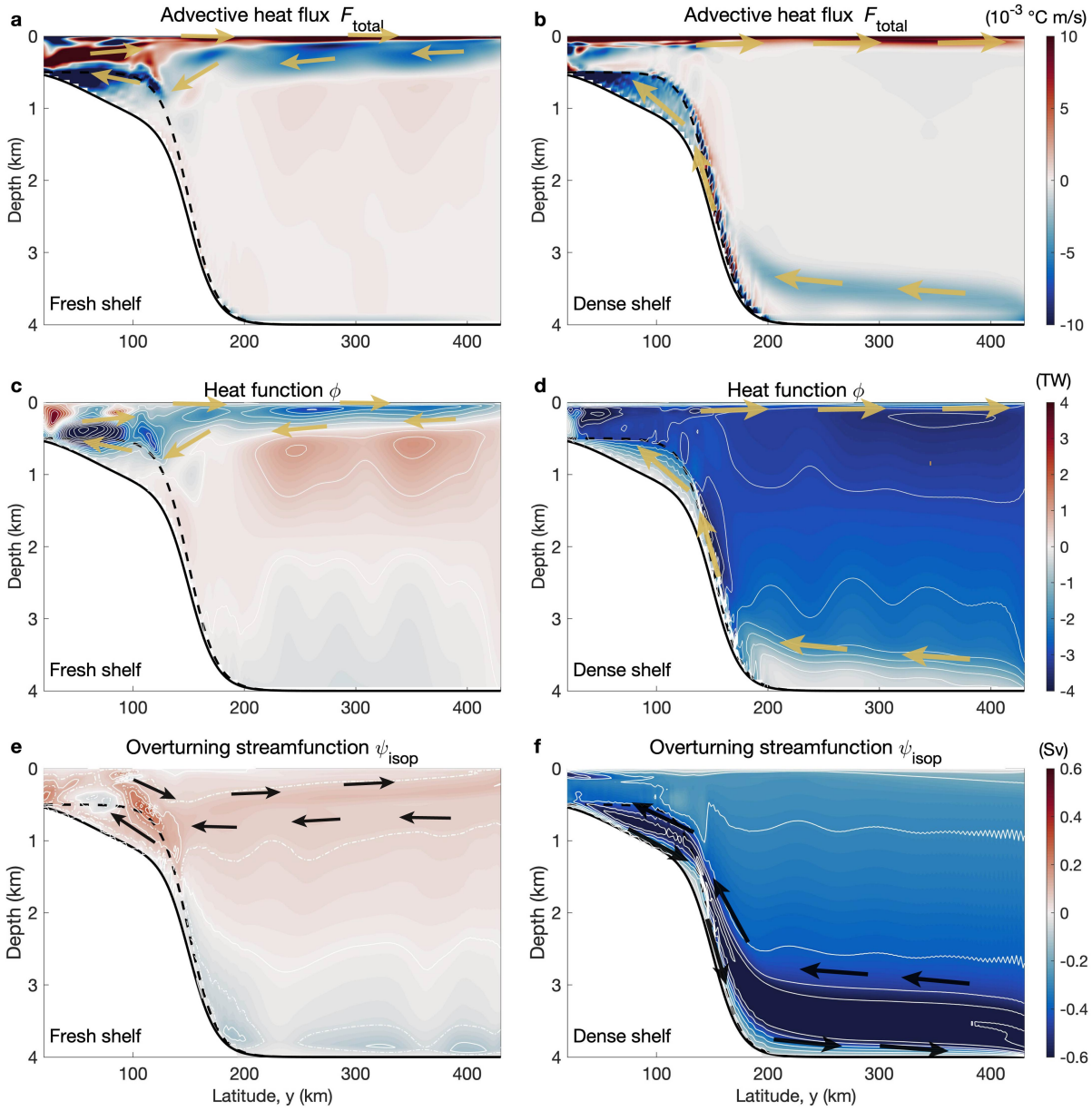

Fig. 3 | Pathways of heat and overturning circulation in the fresh-shelf and dense-shelf cases. a-b, time-mean and zonally integrated meridional advective heat flux. **c-d**, time-mean heat function in TW (1 TW = 10^{12} W). **e-f**, time-mean overturning streamfunction in Sv (1 Sv = 10^6 m^3/s). Yellow arrows denote the pathways of heat, and black arrows denote the direction of the overturning circulation. **a**, **c** and **e**, the fresh-shelf case. **b**, **d** and **f**, the dense-shelf case. The spacings of the color contours in all panels are 1/40 of the corresponding colorbar range. The 20-km sponge layers in the northern and southern boundaries are excluded.

transport increases with steeper continental slope, thinner sea ice, and weaker zonal wind, and exhibits a non-monotonic response to tidal amplitude.

To provide mechanistic insight into the shoreward heat transport in different cases, we show the vertical structure of the advective heat fluxes in Fig. 3a-b, and heat function in Fig. 3c-d. The heat function was first introduced by Boccaletti et al. (2005)[4] to trace the oceanic pathways of heat, which is defined as

$$\phi(y,z) = c_p \rho_0 \int_{z'=\eta_b}^{z} \left\langle \overline{v\theta}^E - \overline{v}^E \theta_{\text{ref}} \right\rangle dz', \qquad (1)$$

where c_p is the specific heat capacity, ρ_0 is the reference density, η_b is the seafloor elevation, v is the meridional velocity, θ is the potential temperature, θ_{ref} is the reference potential temperature, $\overline{\bullet}^E$ denotes an 8-year time average, and the angle brackets denotes zonal integral. The interpretation of the heat function is very similar for different choices of the reference temperature[4], so we use $\theta_{\text{ref}} = 0°C$ in this study for simplicity. Both the heat flux and heat function show that the shoreward heat transport increases near the ocean surface for fresh shelves (Fig. 3a, c), and near the seafloor for dense shelves (Fig. 3b, d).

We find that in either case, the shoreward heat transport is associated with overturning circulation. By vertically integrating meridional transport within potential density layers, we compute

the isopycnal overturning streamfunction[10],

$$\psi_{\mathrm{isop}}(y,\sigma_2) = \overline{\left\langle \int_{z=\eta_b}^{z=0} v\mathcal{H}\left[\sigma_2 - \sigma_2'(x,y,z,t)\right] dz \right\rangle^{E}}, \qquad (2)$$

where σ_2 is the potential density with a reference depth of 2 km, $\sigma_2'(x,y,z,t)$ is the simulated σ_2 field, $z=0$ is the sea surface, and $\mathcal{H}[\cdot]$ is the Heaviside function. We find that for fresh shelves, there is a shallow overturning associated with an export of fresh surface waters (Fig. 3e). For dense shelves, the overturning consists of an export of dense water near the seafloor (Fig. 3f).

In order to understand the relative contribution of tides, transient eddies, and mean flows to shoreward heat transport, we temporally decompose the total heat transport into tidal, eddy, and mean components (see Methods). We find that the shoreward heat flux carried by transient eddies significantly increases over the shelf for both fresh and dense shelves; the tidal heat transport is largely compensated by the mean component, with the residual supporting the heat transport across the continental slope (Extended Data Fig. 3a-c). We further quantify the eddy and tidal heat transport due to the net volume fluxes of water across the slope (namely eddy advection and tidal advection), and due to the mixing of heat along isopycnals (eddy diffusion and tidal diffusion). We show that the heat transport over the shelf is dominated by eddy advection for fresh shelves, and by eddy diffusion for dense shelves (Extended Data Fig. 3d-e). Inspired by the finding that eddy heat transport is essential over the shelf, we analyze the decomposition of the total kinetic energy, and find that the eddy kinetic energy increases substantially for the fresh-shelf and dense-shelf cases (Extended Data Fig. 4). Since the pattern of overturning circulation plays a key role in shoreward heat transport, we also temporally decompose the isopycnal overturning streamfunction into tidal, transient-eddy, Eulerian-mean, and standing-wave components. We find that for fresh shelves, the overturning circulation is dominated by transient baroclinic eddies, with the residual of mean and tidal components accounting for the overturning across the slope (Extended Data Fig. 5). For dense shelves, the overturning circulation is contributed by baroclinic eddies in the open ocean, mean gravity current over the slope, and standing waves in the troughs of the continental shelf (Extended Data Fig. 6).

We find that if the horizontal grid spacing is not fine enough, the model can not properly resolve the positive feedback in the fresh-shelf regime. In contrast, model resolution higher than 2 km (e.g., 1 km) does not qualitatively make any difference (figure not shown). The lines in Fig. 2b show the sensitivity of shoreward heat transport to horizontal grid spacing, with green and yellow lines corresponding to the fresh-shelf and dense-shelf regimes, respectively. For heat transferred onto the shelf (F_{shelf}), the simulations with coarser resolution (5 km or 10 km) are able to capture the increase of shoreward heat transport in the dense-shelf regime. Since shoreward heat transport in the dense-shelf regime is driven by dense water export through canyons[40] (Fig. 3b, f, Extended Data Fig. 6c-d), this suggests that models can capture the heat transport as long as they resolves the canyons on the shelf. However, the coarse-resolution simulations perform poorly in the fresh shelf regime because they do not adequately resolve baroclinic eddies. This is because the first baroclinic Rossby deformation radius[7] (close to 2.3 km over the continental shelf, and 6.8 km in the deep ocean) is relatively small over the shelf and slope. As for the heat transferred onto the slope (F_{slope}) in the fresh-shelf regime, the 5-km and 10-km simulations can capture the trend of F_{slope} with varied shelf bottom salinity (Extended Data Fig. 2b), but the magnitude of the change in F_{slope} is about two times smaller than that in the 2-km simulations. We also find that the standard GM-Redi eddy parameterization scheme is not enough to reproduce the positive feedback, leading to even worse performance in shoreward heat transport (Extended Data Fig. 2), though other sophisticated "slope-aware" eddy parameterization schemes may work[71;70;69].

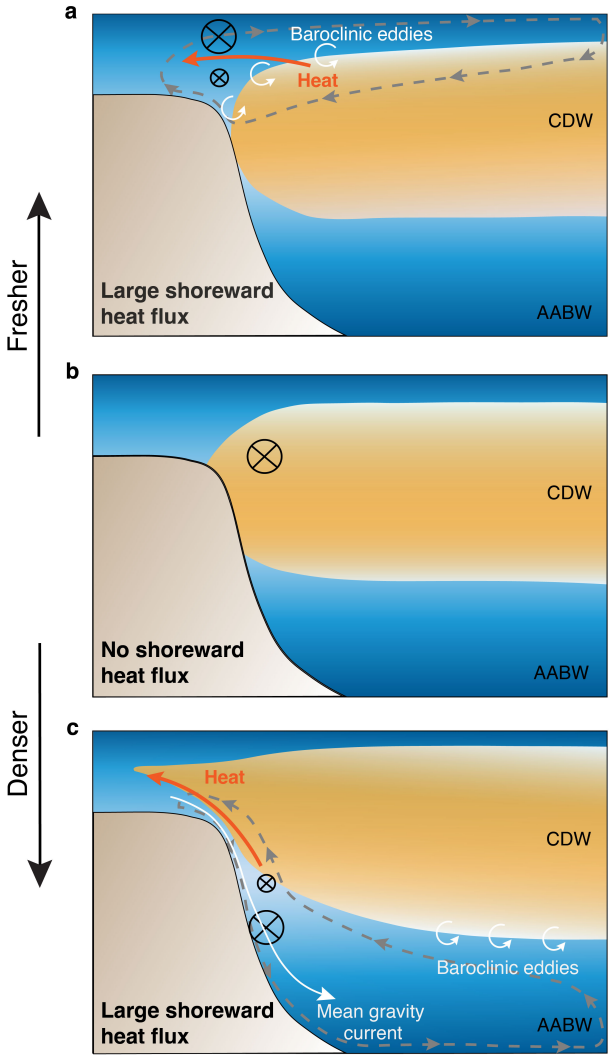

Fig. 4 | Schematic of salinity-controlled shoreward heat transport. The gray dashed curves with arrows denote the zonally averaged meridional overturning circulation. The black circle with a cross shows that the direction of the slope current is westward (into the page), with the size of the circle representing the strength of the slope current. The circular arrows denote the transient baroclinic eddies. In panel **c**, the white curve with an arrow denotes the mean gravity current associated with dense water outflow.

Conclusions and implications

To summarize, we find that both freshening of the fresh shelves and salinification of the dense shelves lead to enhanced heat flux

toward the Antarctic margins. The increased onshore heat transfer with coastal freshening happens only when the horizontal resolution is high enough and thus the model is capable of resolving mesoscale eddies over the shelf and slope (Fig. 2). This suggests that previous studies with relatively coarse-resolution climate models either get the wrong results, or get the right results for the wrong reasons. Fig. 4 schematically summarizes the processes responsible for enhanced shoreward heat transport for fresh shelves and dense shelves. We find that freshening the shelf leads to baroclinic instabilities of the slope front that drive a shallow overturning, bringing warm waters onto the shelf and exporting fresh surface waters offshore (Fig. 4a), while salinifying the shelf leads to dense outflows in canyons that drive a warm return flow at mid-depth (Fig. 4c). These mechanisms of shoreward mass/heat transfer are consistent with the findings of Stewart and Thompson (2016)[63] and Morrison et al. (2020)[40] for dense shelves, Nøst et al. (2011)[44] and Hattermann (2018)[18] for fresh shelves, and previous studies on buoyancy-driven coastal currents in other parts of the ocean[6;72].

This study implies a positive feedback for future climate change: in a warming climate, large volumes of meltwater may increase shoreward heat transport, causing further melt of ice shelves. The enhanced heat transport with weaker zonal winds in the fresh-shelf and dense-shelf cases further implies an increased shoreward heat transport in the future, as weakening easterlies may be expected in the future due to warming over Antarctica and southward shift of the westerlies[57]. Furthermore, our results imply that models with coarse horizontal resolution tend not to capture the enhanced shoreward heat flux in the fresh-shelf regime properly. For future research on ocean heat transport and ice shelf melting, it is essential to employ high-resolution eddy-resolving models and/or improve parameterization schemes for eddy heat flux over the continental shelf and slope.

There are several limitations of this work due to the heavy idealization of the model, which was required to allow adequate resolution of eddies. The model simulates typical winter conditions of the Antarctic margins with permanent sea ice cover, with the assumption that most of the freezing happens south of the model domain, and most of the melt to the north. It does not include seasonal melting and freezing of sea ice, which strongly influence ocean stratification, and thus may modulate shoreward ocean heat transport[76;17]. The parameter regime spanned by the model experiments is not representative of the West Antarctic Peninsula (WAP) where the ice shelves are melting rapidly[48;47], because the model's shelf forcing imposes a strong temperature gradient at the southern boundary that differs from conditions along the WAP. In addition, the idealized channel model is insufficient to understand the circumpolar variability in ocean heat transport and the role of along-slope advection. A high-resolution circumpolar regional model is needed to identify "hot spots" of ocean heat transport around the Antarctic margins, and understand the effect of downstream meltwater advection[16;42]. Moreover, we found that in different shelf salinity regimes, there is a shift in the sensitivity of shoreward heat transport to perturbations of wind, tides, sea ice thickness, and continental slope width. The underlying mechanisms associated with the change in sensitivity require further study.

References

[1] Adusumilli, S., H. A. Fricker, M. R. Siegfried, L. Padman, F. S. Paolo, and S. R. Ligtenberg, 2018: Variable basal melt rates of Antarctic Peninsula ice shelves, 1994–2016. *Geophys. Res. Lett.*, **45 (9)**, 4086–4095, URL https://doi.org/10.1002/2017GL076652.

[2] Bintanja, R., G. J. van Oldenborgh, S. Drijfhout, B. Wouters, and C. Katsman, 2013: Important role for ocean warming and increased ice-shelf melt in Antarctic sea-ice expansion. *Nat. Geosci.*, **6 (5)**, 376–379, URL https://doi.org/10.1126/10.1038/NGEO1767.

[3] Blumsack, S. L., and P. J. Gierasch, 1972: Mars: The effects of topography on baroclinic instability. *J. Atmos. Sci.*, **29 (6)**, 1081–1089, URL https://doi.org/10.1175/1520-0469(1972)029<1081:MTEOTO>2.0.CO;2.

[4] Boccaletti, G., R. Ferrari, A. Adcroft, D. Ferreira, and J. Marshall, 2005: The vertical structure of ocean heat transport. *Geophys. Res. Lett.*, **32 (10)**, URL https://doi.org/10.1029/2005GL022474.

[5] Bronselaer, B., M. Winton, S. M. Griffies, W. J. Hurlin, K. B. Rodgers, O. V. Sergienko, R. J. Stouffer, and J. L. Russell, 2018: Change in future climate due to antarctic meltwater. *Nature*, **564 (7734)**, 53–58, URL https://doi.org/10.1038/s41586-018-0712-z.

[6] Bryden, H. L., D. Halpern, and R. D. Pillsbury, 1980: Importance of eddy heat flux in a heat budget for Oregon coastal waters. *J. Geophys. Res.: Oceans*, **85 (C11)**, 6649–6653, URL https://doi.org/10.1029/JC085iC11p06649.

[7] Chelton, D. B., R. A. DeSzoeke, M. G. Schlax, K. El Naggar, and N. Siwertz, 1998: Geographical variability of the first baroclinic Rossby radius of deformation. *J. Phys. Oceanogr.*, **28 (3)**, 433–460, URL https://doi.org/10.1175/1520-0485(1998)028<0433:GVOTFB>2.0.CO;2.

[8] Danabasoglu, G., and J. C. Mc Williams, 1995: Sensitivity of the global ocean circulation to parameterizations of mesoscale tracer transports. *J. Clim.*, **8 (12)**, 2967–2987, URL https://doi.org/10.1175/1520-0442(1995)008<2967:SOTGOC>2.0.CO;2.

[9] Depoorter, M. A., J. L. Bamber, J. A. Griggs, J. T. Lenaerts, S. R. Ligtenberg, M. R. van den Broeke, and G. Moholdt, 2013: Calving fluxes and basal melt rates of Antarctic ice shelves. *Nature*, **502 (7469)**, 89–92, URL https://doi.org/10.1038/nature12567.

[10] Döös, K., and D. J. Webb, 1994: The Deacon cell and the other meridional cells of the Southern Ocean. *J. Phys. Oceanogr.*, **24 (2)**, 429–442, URL https://doi.org/10.1175/1520-0485(1994)024<0429:TDCATO>2.0.CO;2.

[11] Fer, I., E. Darelius, and K. B. Daae, 2016: Observations of energetic turbulence on the Weddell Sea continental slope. *Geophys. Res. Lett.*, **43 (2)**, 760–766, URL https://doi.org/10.1002/2015GL067349.

[12] Fogwill, C., S. Phipps, C. Turney, and N. Golledge, 2015: Sensitivity of the Southern Ocean to enhanced regional Antarctic ice sheet meltwater input. *Earth's Future*, **3 (10)**, 317–329, URL https://doi.org/10.1002/2015EF000306.

[13] Gent, P. R., and J. C. Mcwilliams, 1990: Isopycnal mixing in ocean circulation models. *J. Phys. Oceanogr.*, **20 (1)**, 150–155, URL https://doi.org/10.1175/1520-0485(1990)020<0150:IMIOCM>2.0.CO;2.

[14] Gent, P. R., J. Willebrand, T. J. McDougall, and J. C. McWilliams, 1995: Parameterizing eddy-induced tracer transports in ocean circulation models. *J. Phys. Oceanogr.*, **25 (4)**, 463–474, URL https://doi.org/10.1175/1520-0485(1995)025<0463:PEITTI>2.0.CO;2.

[15] Golledge, N. R., E. D. Keller, N. Gomez, K. A. Naughten, J. Bernales, L. D. Trusel, and T. L. Edwards, 2019: Global environmental consequences of twenty-first-century ice-sheet melt. *Nature*, **566 (7742)**, 65–72, URL https://doi.org/10.1038/s41586-019-0889-9.

[16] Graham, J. A., K. J. Heywood, C. P. Chavanne, and P. R. Holland, 2013: Seasonal variability of water masses and transport on the Antarctic continental shelf and slope in the southeastern Weddell Sea. *J. Geophys. Res.: Oceans*, **118 (4)**, 2201–2214, URL https://doi.org/10.1002/jgrc.20174.

[17] Hattermann, T., 2018: Antarctic thermocline dynamics along a narrow shelf with easterly winds. *J. Phys. Oceanogr.*, **48 (10)**, 2419–2443, URL https://doi.org/10.1175/JPO-D-18-0064.1.

[18] Hattermann, T., and G. Rohardt, 2018: Kapp Norvegia Antarctic Slope Front climatology. PANGAEA, URL https://doi.org/10.1594/PANGAEA.893199, supplement to: Hattermann, Tore (2018): Antarctic Thermocline Dynamics along a Narrow Shelf with Easterly Winds. J. Phys. Oceanogr., 48(10), 2419-2443, https://doi.org/10.1175/JPO-D-18-0064.1.

[19] Hellmer, H. H., F. Kauker, R. Timmermann, J. Determann, and J. Rae, 2012: Twenty-first-century warming of a large Antarctic ice-shelf cavity by a redirected coastal current. *Nature*, **485 (7397)**, 225–228, URL https://doi.org/10.1038/nature11064.

[20] Hetland, R. D., 2017: Suppression of baroclinic instabilities in buoyancy-driven flow over sloping bathymetry. *J. Phys. Oceanogr.*, **47 (1)**, 49–68, URL https://doi.org/10.1175/JPO-D-15-0240.1.

[21] Heywood, K. J., and Coauthors, 2014: Ocean processes at the Antarctic continental slope. *Philos. Trans. R. Soc. A*, **372 (2019)**, 20130 047, URL https://doi.org/10.1098/rsta.2013.0047.

[22] Hibler, W. D., III, 1979: A dynamic thermodynamic sea ice model. *J. Phys. Oceanogr.*, **9 (4)**, 815–846, URL https://doi.org/10.1175/1520-0485(1979)009<0815:ADTSIM>2.0.CO;2.

[23] Holland, P. R., R. E. Hewitt, and M. M. Scase, 2014: Wave breaking in dense plumes. *J. Phys. Oceanogr.*, **44 (2)**, 790–800, URL https://doi.org/10.1175/JPO-D-13-0110.1.

[24] Isachsen, P. E., 2011: Baroclinic instability and eddy tracer transport across sloping bottom topography: How well does a modified Eady model do in primitive equation simulations? *Ocean Modell.*, **39 (1-2)**, 183–199, URL https://doi.org/10.1016/j.ocemod.2010.09.007.

[25] Jacobs, S., 2006: Observations of change in the Southern Ocean. *Philos. Trans. R. Soc. A*, **364 (1844)**, 1657–1681, URL https://doi.org/10.1098/rsta.2006.1794.

[26] Jacobs, S. S., 1991: On the nature and significance of the Antarctic Slope Front. *Mar. Chem.*, **35 (1-4)**, 9–24, URL https://doi.org/10.1016/S0304-4203(09)90005-6.

[27] Jacobs, S. S., and C. F. Giulivi, 2010: Large multidecadal salinity trends near the Pacific–Antarctic continental margin. *J. Clim.*, **23 (17)**, 4508–4524, URL https://doi.org/10.1175/2010JCLI3284.1.

[28] King, M. A., R. J. Bingham, P. Moore, P. L. Whitehouse, M. J. Bentley, and G. A. Milne, 2012: Lower satellite-gravimetry estimates of Antarctic sea-level contribution. *Nature*, **491 (7425)**, 586–589, URL https://doi.org/10.1038/nature11621.

[29] Kusahara, K., and K. I. Ohshima, 2014: Kelvin waves around Antarctica. *J. Phys. Oceanogr.*, **44 (11)**, 2909–2920, URL https://doi.org/10.1175/JPO-D-14-0051.1.

[30] Le Paih, N., T. Hattermann, O. Boebel, T. Kanzow, C. Lüpkes, G. Rohardt, V. Strass, and S. Herbette, 2020: Coherent seasonal acceleration of the Weddell sea boundary current system driven by upstream winds. *J. Geophys. Res. Oceans*, **125 (10)**, e2020JC016 316, URL https://doi.org/10.1029/2020JC016316.

[31] Locarnini, M., and Coauthors, 2018: World Ocean Atlas 2018, Volume 1: Temperature. URL https://www.ncei.noaa.gov/products/world-ocean-atlas.

[32] Loder, J. W., 1980: Topographic rectification of tidal currents on the sides of Georges Bank. *J. Phys. Oceanogr.*, **10 (9)**, 1399–1416, URL https://doi.org/10.1175/1520-0485(1980)010<1399:TROTCO>2.0.CO;2.

[33] Losch, M., D. Menemenlis, J.-M. Campin, P. Heimbach, and C. Hill, 2010: On the formulation of sea-ice models. Part 1: Effects of different solver implementations and parameterizations. *Ocean Modell.*, **33 (1)**, 129–144, URL https://doi.org/10.1016/j.ocemod.2009.12.008.

[34] Marshall, J., A. Adcroft, C. Hill, L. Perelman, and C. Heisey, 1997: A finite-volume, incompressible Navier Stokes model for studies of the ocean on parallel computers. *J. Geophys. Res.*, **102**, 5753–5766, URL https://doi.org/10.1029/96JC02775.

[35] Marshall, J., C. Hill, L. Perelman, and A. Adcroft, 1997: Hydrostatic, quasi-hydrostatic, and nonhydrostatic ocean modeling. *J. Geophys. Res.*, **102**, 5733–5752, URL https://doi.org/10.1029/96JC02776.

[36] McDougall, T. J., D. R. Jackett, D. G. Wright, and R. Feistel, 2003: Accurate and computationally efficient algorithms for potential temperature and density of seawater. *J. Atmos. Oceanic Technol.*, **20 (5)**, 730–741, URL https://doi.org/10.1175/1520-0426(2003)20<730:AACEAF>2.0.CO;2.

[37] Meijers, A., 2014: The Southern Ocean in the coupled model intercomparison project phase 5. *Philos. Trans. R. Soc. A*, **372 (2019)**, 20130 296, URL https://doi.org/10.1098/rsta.2013.0296.

[38] Menviel, L., A. Timmermann, O. E. Timm, and A. Mouchet, 2010: Climate and biogeochemical response to a rapid melting of the West Antarctic Ice Sheet during interglacials and implications for future climate. *Paleoceanography*, **25 (4)**, URL https://doi.org/10.1029/2009PA001892.

[39] Moorman, R., A. K. Morrison, and A. McC. Hogg, 2020: Thermal Responses to Antarctic Ice Shelf Melt in an Eddy-Rich Global Ocean–Sea Ice Model. *J. Climate*, **33 (15)**, 6599–6620, URL https://doi.org/10.1175/JCLI-D-19-0846.1.

[40] Morrison, A., A. M. Hogg, M. H. England, and P. Spence, 2020: Warm Circumpolar Deep Water transport toward Antarctica driven by local dense water export in canyons. *Sci. Adv.*, **6 (18)**, eaav2516, URL https://doi.org/10.1126/sciadv.aav2516.

[41] Muench, R., L. Padman, A. Gordon, and A. Orsi, 2009: A dense water outflow from the Ross Sea, Antarctica: Mixing and the contribution of tides. *J. Mar. Syst.*, **77 (4)**, 369–387, URL https://doi.org/10.1016/j.jmarsys.2008.11.003.

[42] Nakayama, Y., R. Timmermann, C. B. Rodehacke, M. Schröder, and H. H. Hellmer, 2014: Modeling the spreading of glacial meltwater from the Amundsen and Bellingshausen Seas. *Geophys. Res. Lett.*, **41 (22)**, 7942–7949, URL https://doi.org/10.1002/2014GL061600.

[43] Nakayama, Y., and Coauthors, 2021: Antarctic Slope Current modulates ocean heat intrusions towards Totten Glacier. *Geophys. Res. Lett.*, **48 (17)**, e2021GL094 149, URL https://doi.org/10.1029/2021GL094149.

[44] Nøst, O. A., M. Biuw, V. Tverberg, C. Lydersen, T. Hattermann, Q. Zhou, L. H. Smedsrud, and K. M. Kovacs, 2011: Eddy overturning of the Antarctic Slope Front controls glacial melting in the Eastern Weddell Sea. *J. Geophys. Res*, **116**, C11 014, URL https://doi.org/10.1029/2011JC006965.

[45] Nurser, A. G., and M.-M. Lee, 2004: Isopycnal averaging at constant height. Part II: Relating to the residual streamfunction in Eulerian space. *J. Phys. Oceanogr.*, **34 (12)**, 2740–2755, URL https://doi.org/10.1175/JPO2650.1.

[46] Padman, L., S. L. Howard, A. H. Orsi, and R. D. Muench, 2009: Tides of the northwestern Ross Sea and their impact on dense outflows of Antarctic Bottom Water. *Deep Sea Res. Part II*, **56 (13)**, 818–834, URL https://doi.org/10.1016/j.dsr2.2008.10.026.

[47] Paolo, F. S., H. A. Fricker, and L. Padman, 2015: Volume loss from Antarctic ice shelves is accelerating. *Science*, **348 (6232)**, 327–331, URL https://doi.org/10.1126/science.aaa0940.

[48] Pritchard, H., S. R. Ligtenberg, H. A. Fricker, D. G. Vaughan, M. R. van den Broeke, and L. Padman, 2012: Antarctic ice-sheet loss driven by basal melting of ice shelves. *Nature*, **484 (7395)**, 502–505, URL https://doi.org/10.1038/nature10968.

[49] Redi, M. H., 1982: Oceanic isopycnal mixing by coordinate rotation. *J. Phys. Oceanogr.*, **12 (10)**, 1154–1158, URL https://doi.org/10.1175/1520-0485(1982)012<1154:OIMBCR>2.0.CO;2.

[50] Sadai, S., A. Condron, R. DeConto, and D. Pollard, 2020: Future climate response to Antarctic Ice Sheet melt caused by anthropogenic warming. *Sci. Adv.*, **6 (39)**, eaaz1169, URL https://doi.org/10.1126/sciadv.aaz1169.

[51] Sallée, J.-B., 2018: Southern ocean warming. *Oceanography*, **31 (2)**, 52–62, URL https://www.jstor.org/stable/26542651.

[52] Schloesser, F., T. Friedrich, A. Timmermann, R. M. DeConto, and D. Pollard, 2019: Antarctic iceberg impacts on future Southern Hemisphere climate. *Nat. Clim. Change*, **9 (9)**, 672–677, URL https://doi.org/10.1038/s41558-019-0546-1.

[53] Schmidtko, S., K. J. Heywood, A. F. Thompson, and S. Aoki, 2014: Multidecadal warming of Antarctic waters. *Science*, **346 (6214)**, 1227–1231, URL https://doi.org/10.1126/science.1256117.

[54] Si, Y., A. Stewart, and I. Eisenman, submitted: Coupled ocean/sea ice dynamics of the antarctic slope current driven by topographic eddy suppression and sea ice momentum redistribution. *J. Phys. Oceanogr.*, URL https://doi.org/10.1002/essoar.10507558.1.

[55] Smagorinsky, J., 1963: General circulation experiments with the primitive equations: I. The basic experiment. *Mon. Weather Rev.*, **91 (3)**, 99–164, URL https://doi.org/10.1175/1520-0493(1963)091<0099:GCEWTP>2.3.CO;2.

[56] Smagorinsky, J., 1993: Some historical remarks on the use of nonlinear viscosities. *Evolution of Physical Oceanography*, B. Galperin, and S. Orszag, Eds., Cambridge University Press, 3–36.

[57] Spence, P., S. M. Griffies, M. H. England, A. M. Hogg, O. A. Saenko, and N. C. Jourdain, 2014: Rapid subsurface warming and circulation changes of Antarctic coastal waters by poleward shifting winds. *Geophys. Res. Lett.*, **41 (13)**, 4601–4610, URL https://doi.org/10.1002/2014GL060613.

[58] Spence, P., R. M. Holmes, A. M. Hogg, S. M. Griffies, K. D. Stewart, and M. H. England, 2017: Localized rapid warming of West Antarctic subsurface waters by remote winds. *Nat. Clim. Change*, **7 (8)**, 595–603, URL https://doi.org/10.1038/NCLIMATE3335.

[59] St-Laurent, P., J. M. Klinck, and M. S. Dinniman, 2013: On the role of coastal troughs in the circulation of warm circumpolar deep water on Antarctic shelves. *J. Phys. Oceanogr.*, **43 (1)**, 51–64, URL https://doi.org/10.1175/JPO-D-11-0237.1.

[60] Stewart, A. L., A. Klocker, and D. Menemenlis, 2018: Circum-Antarctic shoreward heat transport derived from an eddy-and tide-resolving simulation. *Geophys. Res. Lett.*, **45 (2)**, 834–845, URL https://doi.org/10.1002/2017GL075677.

[61] Stewart, A. L., A. Klocker, and D. Menemenlis, 2019: Acceleration and overturning of the Antarctic Slope Current by winds, eddies, and tides. *J. Phys. Oceanogr.*, **49 (8)**, 2043–2074, URL https://doi.org/10.1175/JPO-D-18-0221.1.

[62] Stewart, A. L., and A. F. Thompson, 2015: Eddy-mediated transport of warm Circumpolar Deep Water across the Antarctic Shelf Break. *Geophys. Res. Lett.*, **42**, 432–440, URL https://doi.org/10.1002/2014GL062281.

[63] Stewart, A. L., and A. F. Thompson, 2016: Eddy generation and jet formation via dense water outflows across the Antarctic continental slope. *J. Phys. Oceanogr.*, **46 (12)**, 3729–3750, URL https://doi.org/10.1175/JPO-D-16-0145.1.

[64] Swart, N. C., S. T. Gille, J. C. Fyfe, and N. P. Gillett, 2018: Recent Southern Ocean warming and freshening driven by greenhouse gas emissions and ozone depletion. *Nat. Geosci.*, **11 (11)**, 836–841, URL https://doi.org/10.1038/s41561-018-0226-1.

[65] Swingedouw, D., T. Fichefet, P. Huybrechts, H. Goosse, E. Driesschaert, and M.-F. Loutre, 2008: Antarctic ice-sheet melting provides negative feedbacks on future climate warming. *Geophys. Res. Lett.*, **35 (17)**, URL https://doi.org/10.1029/2008GL034410.

[66] Thompson, A. F., K. J. Heywood, S. Schmidtko, and A. L. Stewart, 2014: Eddy transport as a key component of the Antarctic overturning circulation. *Nat. Geosci.*, **7 (12)**, 879–884, URL https://doi.org/10.1038/ngeo2289.

[67] Thompson, A. F., A. L. Stewart, P. Spence, and K. J. Heywood, 2018: The Antarctic Slope Current in a changing climate. *Rev. Geophys.*, **56 (4)**, 741–770, URL https://doi.org/10.1029/2018RG000624.

[68] Towns, J., and Coauthors, 2014: XSEDE: Accelerating scientific discovery. *Comput. Sci. Eng.*, **16 (5)**, 62–74, URL https://doi.org/10.1109/MCSE.2014.80.

[69] Wang, Y., and A. L. Stewart, 2018: Eddy dynamics over continental slopes under retrograde winds: Insights from a model inter-comparison. *Ocean Modell.*, **121**, 1–18, URL https://doi.org/10.1016/j.ocemod.2017.11.006.

[70] Wang, Y., and A. L. Stewart, 2020: Scalings for eddy buoyancy transfer across continental slopes under retrograde winds. *Ocean Modell.*, **147**, 101 579, URL https://doi.org/10.1016/j.ocemod.2020.101579.

[71] Wei, H., and Y. Wang, 2021: Full-depth scalings for isopycnal eddy mixing across continental slopes under upwelling-favorable winds. *J. Adv. Model. Earth Syst.*, e2021MS002498, URL https://doi.org/10.1029/2021MS002498.

[72] Whitney, F., W. Crawford, and P. Harrison, 2005: Physical processes that enhance nutrient transport and primary productivity in the coastal and open ocean of the subarctic NE Pacific. *Deep Sea Res. Part II*, **52 (5-6)**, 681–706, URL https://doi.org/10.1016/j.dsr2.2004.12.023.

[73] Whitworth, T., and A. H. Orsi, 2006: Antarctic Bottom Water production and export by tides in the Ross Sea. *Geophys. Res. Lett.*, **33 (12)**, URL https://doi.org/10.1029/2006GL026357.

[74] Whitworth, T., III, A. H. Orsi, S.-J. Kim, W. D. Nowlin Jr, and R. A. Locarnini, 1985: Water masses and mixing near the Antarctic Slope Front. *Ocean, ice, and atmosphere: interactions at the Antarctic continental margin*, **75**, 1–27, URL https://doi.org/10.1029/AR075p0001.

[75] Winton, M., 2000: A reformulated three-layer sea ice model. *J. Atmos. Oceanic Technol.*, **17 (4)**, 525–531, URL https://doi.org/10.1175/1520-0426(2000)017<0525:ARTLSI>2.0.CO;2.

[76] Zhou, Q., T. Hattermann, O. Nøst, M. Biuw, K. Kovacs, and C. Lydersen, 2014: Wind-driven spreading of fresh surface water beneath ice shelves in the Eastern Weddell Sea. *J. Geophys. Res.: Oceans*, **119 (6)**, 3818–3833, URL http://dx.doi.org/10.1002/2013JC009556.

[77] Zweng, M., and Coauthors, 2019: World Ocean Atlas 2018, Volume 2: Salinity. URL https://www.ncei.noaa.gov/products/world-ocean-atlas.

Data availability

The products that we calculated from MITgcm_ASF diagnostics and the data we used to make figures for this manuscript are available at: http://doi.org/10.5281/zenodo.5915019. All the raw data of the model output are available at: https://research.aos.ucla.edu/ysi/MITgcm_ASF_heat_transport_exps.

Code availability

The source code of the Massachusetts Institute of Technology General Circulation Model (MITgcm) is available at: http://mitgcm.org. The Matlab scripts used to generate, run, and analyze the MITgcm simulations, as well as the experiment configurations are available at: http://doi.org/10.5281/zenodo.5915019.

Acknowledgement

This work is supported by the National Science Foundation, under award numbers OCE-1751386 and OPP-2023244, as well as awards OCE-2048590 and OPP-1643445. This work used the Extreme Science and Engineering Discovery Environment XSEDE[68], which is supported by the National Science Foundation grant number ACI-1548562. This work also used the Hoffman2 Cluster, which is supported by the IDRE Research Technology Group at UCLA. We thank the MITgcm team for their contribution to numerical modeling and for making their code available. Y. Si acknowledges the scholarship provided by China Scholarship Council that supports her study at UCLA.

Author contributions

Y.S. and A.L.S. developed the model, designed the experiments and analysis. I.E. assisted in the model development and the design of the analysis. Y.S. conducted the experiments and analysis, and wrote the manuscript. A.L.S. and I.E. contributed to the interpretation of the results and assisted in the writing.

Competing interests

The authors declare no competing interests

Methods

Model configuration and simulations

In this study, we use the restoring salinity at the southern boundary as a control parameter. For the reference simulation, the surface salinity of the southern boundary is set to be the same as the surface salinity of the northern boundary (34.12 psu); the bottom salinity of the southern boundary (shelf bottom salinity) is selected to make sure there is no dense water formation over the shelf, i.e., the potential density with a reference pressure of 4 km (σ_4) at the bottom of the continental shelf ($y = 0$ km, $z = -500$ m) is identical to that at the seafloor of the northern boundary ($y = 450$ km, $z = -4000$ m). For simulations with shelf salinity fresher than the reference case ("fresh-shelf regime"), we use a vertically uniform salinity profile at the southern boundary. For simulations with shelf salinity salter than the reference case ("dense-shelf regime"), we set surface salinity to be 34.12 psu, and then increase salinity linearly with depth. We set the restoring salinity in this way according to the climatology (Fig. 1b, c), i.e., large vertical variation of shelf salinity in the dense-shelf regime, and much smaller vertical variation of shelf salinity in the fresh-shelf regime. The model is forced by fixed atmospheric state. Both the zonal and meridional winds are strongest at the southern boundary ($y = 0$ km), decreasing linearly offshore with zero wind speeds at the northern boundary ($y = 450$ km). In addition, we prescribe a barotropic tidal current in the meridional direction normal to the northern and southern boundaries, with an idealized tidal period of 12 hours. Due to mass conservation, the tidal current amplitude over the shelf is about 8 times larger than that in the deep ocean[32]. For a detailed description of model bathymetry, atmospheric state, tides, sea ice, initial and boundary conditions, viscosity and diffusivity, please see Si et al. (submitted)[54].

In contrast to Si et al. (submitted)[54], we use the Smagorinsky viscosity[55;56] in all the simulations of this study. We turn off the grid-dependent biharmonic viscosities, and set the non-dimensional Smagorinsky biharmonic viscosity factor to 4. In addition, we apply standard GM-Redi eddy parameterization[13;14;49] for simulations with horizontal grid spacing of 5 km or 10 km. The isopycnal diffusivity and thickness diffusivity are set to 100 m^2/s. The maximum isopycnal slope is 0.025. The DM95 tapering scheme[8] is activated for these simulations, with DM95 critical slope 0.025 and DM95 tapering width 0.0025. The gray lines in Extended Data Fig. 2 show that the straightforward application of GM-Redi parameterization can not correctly capture the onshore heat transport. We experimented with additional combinations of GM-Redi parameters, not reported here, but were unable to obtain an improved representation of the onshore heat transport.

Extended Data Table 1 shows the list of experiments. Seven model parameters are varied: 1) shelf salinity profile, including the restoring salinity at the sea surface ($S^{\text{surf}}_{\text{south}}$) and the seafloor ($S^{\text{bot}}_{\text{south}}$) of the continental shelf at the southern boundary; 2) zonal wind speed at the southern boundary (U_{a0}); 3) meridional wind speed at the southern boundary (V_{a0}); 4) barotropic tidal current amplitude (A_{tide}) at the northern boundary; 5) restoring sea ice thickness (h_{i0}) at the southern boundary; 6) continental slope width (W_S); 7) horizontal grid spacing (Δ_x, Δ_y).

Extended Data Fig. 1 shows the time- and zonal-mean zonal circulation in the fresh-shelf, reference, and dense-shelf cases, overlaid by neutral density contours. Same as reported by previous studies[30;54], the slope current is surface-intensified in the fresh-shelf case (Extended Data Fig. 1a), nearly barotropic in the reference case (Extended Data Fig. 1b), and bottom-intensified in the dense-shelf case (Extended Data Fig. 1c). Undercurrents appear for large salinity gradients, flowing eastward in the fresh-shelf and dense-shelf cases.

Operators for temporal decomposition

In order to calculate temporal decomposition of shoreward heat transport, overturning streamfunction, and kinetic energy, we define two time-averages over a single day ($\overline{\bullet}^T$) and over the analysis period ($\overline{\bullet}^E$)[60;61],

$$\overline{\bullet}^T = \frac{1}{1\text{ day}}\int_{t_0}^{t_0+1\text{ day}} \bullet\, dt, \quad \overline{\bullet}^E = \frac{1}{8\text{ years}}\int_{t_0}^{t_0+8\text{ years}} \overline{\bullet}^T\, dt. \tag{3}$$

These operators allows us to decompose any simulation variable into mean (ξ_m), eddy (ξ_e), and tidal (ξ_t) components:

$$\xi_m = \overline{\overline{\xi}^T}^E = \overline{\xi}^E, \quad \xi_e = \overline{\xi}^T - \overline{\xi}^E, \quad \xi_t = \xi - \xi_m - \xi_e = \xi - \overline{\xi}^T, \tag{4}$$

where ξ represents velocity $\boldsymbol{u} = (u,\ v,\ w)$, potential temperature θ, or potential density σ_2 with a reference depth of 2 km.

Decomposition of the total meridional heat transport

The total meridional heat transport in the ocean is mostly contributed by the advective heat transport. Following Stewart et al. (2018)[60], we temporally decompose the total meridional advective heat flux (F_{total}) into mean (F_{mean}), eddy (F_{eddy}), and tidal (F_{tide}) components, i.e., $F_{\text{total}} = F_{\text{mean}} + F_{\text{eddy}} + F_{\text{tide}}$.

$$F_{\text{total}} = \overline{v\theta}^E, \tag{5a}$$

$$F_{\text{mean}} = v_m\theta_m, \tag{5b}$$

$$F_{\text{eddy}} = \overline{v_e\theta_e}^E = \overline{\overline{v}^T\overline{\theta}^T}^E - F_{\text{mean}}, \tag{5c}$$

$$F_{\text{tide}} = \overline{v_t\theta_t}^E = F_{\text{total}} - \overline{\overline{v}^T\overline{\theta}^T}^E. \tag{5d}$$

Extended Data Fig. 3 shows the zonally and vertically integrated meridional advective heat fluxes. In all cases, the shoreward tidal heat transport is largely compensated by the offshore mean component, which is consistent with Stewart et al. (2018)[60]. The residual of the mean and tidal components comprises the heat transport near the shelf break. Relative to the reference case, the eddy heat transport is enhanced over the shelf and in the deep ocean in both the fresh-shelf and dense-shelf cases. Near the continental shelf break, the eddy heat transport is weaker because the baroclinic eddies are suppressed there by the topographic vorticity gradient[3;24;20].

Decomposition of the total kinetic energy

The total kinetic energy (KE) is decomposed into mean (MKE), eddy (EKE), and tidal (TKE) components, i.e., KE = MKE + EKE + TKE.

$$\text{KE} = \frac{1}{2}\overline{\boldsymbol{u}^2}^E, \tag{6a}$$

$$\text{MKE} = \frac{1}{2}\overline{\boldsymbol{u}_m^2}^E, \tag{6b}$$

$$\text{EKE} = \frac{1}{2}\overline{\boldsymbol{u}_e^2}^E = \frac{1}{2}\overline{(\overline{\boldsymbol{u}}^T)^2}^E - \text{MKE}, \tag{6c}$$

$$\text{TKE} = \frac{1}{2}\overline{\boldsymbol{u}_t^2}^E = \text{KE} - \frac{1}{2}\overline{(\overline{\boldsymbol{u}}^T)^2}^E. \tag{6d}$$

We find that the EKE increases greatly when the continental shelves are very salty or very fresh, while the magnitudes of the MKE and TKE do not change much across the simulations with varying shelf salinity (Extended Data Fig. 4a-c). For fresh shelves, the zonally integrated EKE is enhanced near the surface (Extended Data Fig. 4d). For dense shelves, the zonally integrated EKE is enhanced over the slope, and in the deep ocean (Extended Data Fig. 4f).

Decomposition of the isopycnal overturning streamfunction

As noted in the main text, the shoreward heat transport is closely related to the meridional overturning circulation. We investigate to what extent different components of the flow contribute to the overturning circulation by decomposing the isopycnal overturning streamfunction ($\psi_{\rm isop}$) into mean ($\psi_{\rm mean}$), transient-eddy ($\psi_{\rm eddy}$) and tidal ($\psi_{\rm tide}$) components, i.e., $\psi_{\rm isop} = \psi_{\rm mean} + \psi_{\rm eddy} + \psi_{\rm tide}$. We calculate the overturning streamfunction in potential density σ_2-coordinate, and then remap it to z-coordinate following the standard approach[45].

$$\psi_{\rm isop}(y,\sigma_2) = \left\langle \overline{\int_{z=\eta_b}^{z=0} v\mathcal{H}\Big[\sigma_2 - \sigma_2'(x,y,z,t)\Big]dz}^{E} \right\rangle, \tag{7a}$$

$$\psi_{\rm mean}(y,\sigma_2) = \left\langle \int_{z=\eta_b}^{z=0} v_m\mathcal{H}\Big[\sigma_2 - \sigma_{2m}'(x,y,z)\Big]dz \right\rangle, \tag{7b}$$

$$\begin{aligned}\psi_{\rm eddy}(y,\sigma_2) &= \left\langle \overline{\int_{z=\eta_b}^{z=0} v_e\mathcal{H}\Big[\sigma_2 - \sigma_{2e}'(x,y,z,t)\Big]dz}^{E} \right\rangle \\ &= \left\langle \overline{\int_{z=\eta_b}^{z=0} \overline{v}^T\mathcal{H}\Big[\sigma_2 - \overline{\sigma_2'(x,y,z,t)}^T\Big]dz}^{E} \right\rangle - \psi_{\rm mean}(y,\sigma_2),\end{aligned} \tag{7c}$$

$$\begin{aligned}\psi_{\rm tide}(y,\sigma_2) &= \left\langle \overline{\int_{z=\eta_b}^{z=0} v_t\mathcal{H}\Big[\sigma_2 - \sigma_{2t}'(x,y,z,t)\Big]dz}^{E} \right\rangle \\ &= \psi_{\rm isop}(y,\sigma_2) - \left\langle \overline{\int_{z=\eta_b}^{z=0} \overline{v}^T\mathcal{H}\Big[\sigma_2 - \overline{\sigma_2'(x,y,z,t)}^T\Big]dz}^{E} \right\rangle,\end{aligned} \tag{7d}$$

where primes ($'$) denote simulated field, $\mathcal{H}[\cdot]$ is the Heaviside function, and the angle brackets denote the zonal integral. We further decompose the mean overturning streamfunction into Eulerian-mean ($\psi_{\rm EM}$) and standing-wave ($\psi_{\rm SW}$, also referred to as "standing-eddy") components, i.e., $\psi_{\rm mean} = \psi_{\rm SW} + \psi_{\rm EM}$.

$$\psi_{\rm EM}(y,\sigma_2) = \int_{z=\eta_b}^{z=0} \langle v_m\rangle\mathcal{H}\Big[\sigma_2 - \langle\sigma_{2m}(x,y,z)\rangle\Big]dz, \tag{8a}$$

$$\psi_{\rm SW}(y,\sigma_2) = \psi_{\rm mean}(y,\sigma_2) - \psi_{\rm EM}(y,\sigma_2). \tag{8b}$$

Extended Data Figs. 5 and 6 show the temporal decomposition of the isopycnal overturning streamfunction for fresh and dense shelves. For fresh shelves, there is a subsurface, baroclinic, eddy-driven overturning over the continental shelf and in the open ocean (Extended Data Fig. 5f); the tidal overturning is approximately compensated by the Eulerian-mean overturning, with the residual supporting the overturning across the continental slope (Extended Data Fig. 5e, c). For dense shelves, the transient eddies dominate the overturning in the deep ocean (Extended Data Fig. 6f); gravity currents comprise the Eulerian-mean component over the slope (Extended Data Fig. 6c) where eddies are suppressed; the standing eddy component becomes important in the troughs on the continental shelf (Extended Data Fig. 6d).

Diffusion and advection by tides and eddies

Following Stewart and Thompson (2016)[63], we further decompose the meridional eddy and tidal heat transports into tidal advection, tidal diffusion, eddy advection and eddy diffusion,

$$F^{\rm adv}_{\rm eddy} = v_{\rm eddy}\overline{\theta}^E,\ F^{\rm adv}_{\rm tide} = v_{\rm tide}\overline{\theta}^E \tag{9a}$$

$$F^{\rm diffusion}_{\rm eddy} = F_{\rm eddy} - F^{\rm adv}_{\rm eddy},\ F^{\rm diffusion}_{\rm tide} = F_{\rm tide} - F^{\rm adv}_{\rm tide}, \tag{9b}$$

where $v_{\rm eddy} = -\partial\tilde{\psi}_{\rm eddy}/\partial z$ and $v_{\rm tide} = -\partial\tilde{\psi}_{\rm tide}/\partial z$, and $\tilde{\psi}$ denotes streamfunctions mapped back to (y,z) space[45]. Eddy advection and tidal advection quantify the cross-slope heat transport associated with the net volume fluxes of water across the slope. The eddy and tidal diffusion quantify the mixing of heat along isopycnals, which need not to be associated with any net volume flux[63].

Extended Data Fig. 3d-e shows eddy/tidal diffusion and advection in the fresh-shelf and dense-shelf cases. For fresh shelves, tidal advection and eddy advection are much larger than the diffusive terms (Extended Data Fig. 3d), indicating that for fresh shelves, the heat transport is due to net freshwater export. For dense shelves, the eddy advection dominates the heat transport in the deep ocean; while over the continental shelf, the eddy heat transport is due to eddy diffusion (Extended Data Fig. 3e).

Δ_x, Δ_y (km)	$S^{\mathrm{surf}}_{\mathrm{south}}$ (psu)	$S^{\mathrm{bot}}_{\mathrm{south}}$ (psu)	U_{a0} (m/s)	V_{a0} (m/s)	A_{tide} (m/s)	h_{i0} (m)	W_S (km)
2, 5, 10	**33**	**33**	**-6**	**6**	**0.05**	**1.0**	**50**
2	33.28	33.28	-6	6	0.05	1.0	50
2, 5, 10	33.56	33.56	-6	6	0.05	1.0	50
2, 5, 10	34.12	34.12	-6	6	0.05	1.0	50
2, 5, 10	**34.12**	**34.12+ΔS**	**-6**	**6**	**0.05**	**1.0**	**50**
2, 5, 10	34.12	34.12+2ΔS	-6	6	0.05	1.0	50
2	34.12	34.12+2.5ΔS	-6	6	0.05	1.0	50
2, 5, 10	**34.12**	**34.12+3ΔS**	**-6**	**6**	**0.05**	**1.0**	**50**
2	33, 34.12	33, 34.12+ΔS, 34.12+3ΔS	**-4**	6	0.05	1.0	50
2	33, 34.12	33, 34.12+ΔS, 34.12+3ΔS	**-8**	6	0.05	1.0	50
2	33, 34.12	33, 34.12+ΔS, 34.12+3ΔS	-6	**4**	0.05	1.0	50
2	33, 34.12	33, 34.12+ΔS, 34.12+3ΔS	-6	**12**	0.05	1.0	50
2	33, 34.12	33, 34.12+ΔS, 34.12+3ΔS	-6	6	**0.00**	1.0	50
2	33, 34.12	33, 34.12+ΔS, 34.12+3ΔS	-6	6	**0.10**	1.0	50
2	33, 34.12	33, 34.12+ΔS, 34.12+3ΔS	-6	6	0.05	**0.2**	50
2	33, 34.12	33, 34.12+ΔS, 34.12+3ΔS	-6	6	0.05	**1.8**	50
2	33, 34.12	33, 34.12+ΔS, 34.12+3ΔS	-6	6	0.05	1.0	**25**
2	33, 34.12	33, 34.12+ΔS, 34.12+3ΔS	-6	6	0.05	1.0	**100**

Extended Data Table 1 | **List of experiments.** Δ_x and Δ_y are the horizontal grid spacings in the zonal and meridional direction, respectively. $\Delta S = 0.23$ psu is the vertical difference in the restoring salinity at the southern boundary between the sea surface ($S^{\mathrm{surf}}_{\mathrm{south}}$) and the seafloor of the continental shelf (500 m depth, $S^{\mathrm{bot}}_{\mathrm{south}}$) of the reference case. U_{a0} and V_{a0} are the zonal (along-slope, positive eastward) and meridional (cross-slope, positive northward) wind speed at the southern boundary, respectively. A_{tide} is the prescribed barotropic tidal current amplitude at the northern boundary. h_{i0} is the restoring sea ice thickness at the southern boundary, which is also the initial sea ice thickness across the domain. W_S is the continental slope width. The boldface shows the three experiments mainly described in this article (the fresh-shelf, reference, and dense-shelf cases), as well as perturbation simulations.

Extended Data

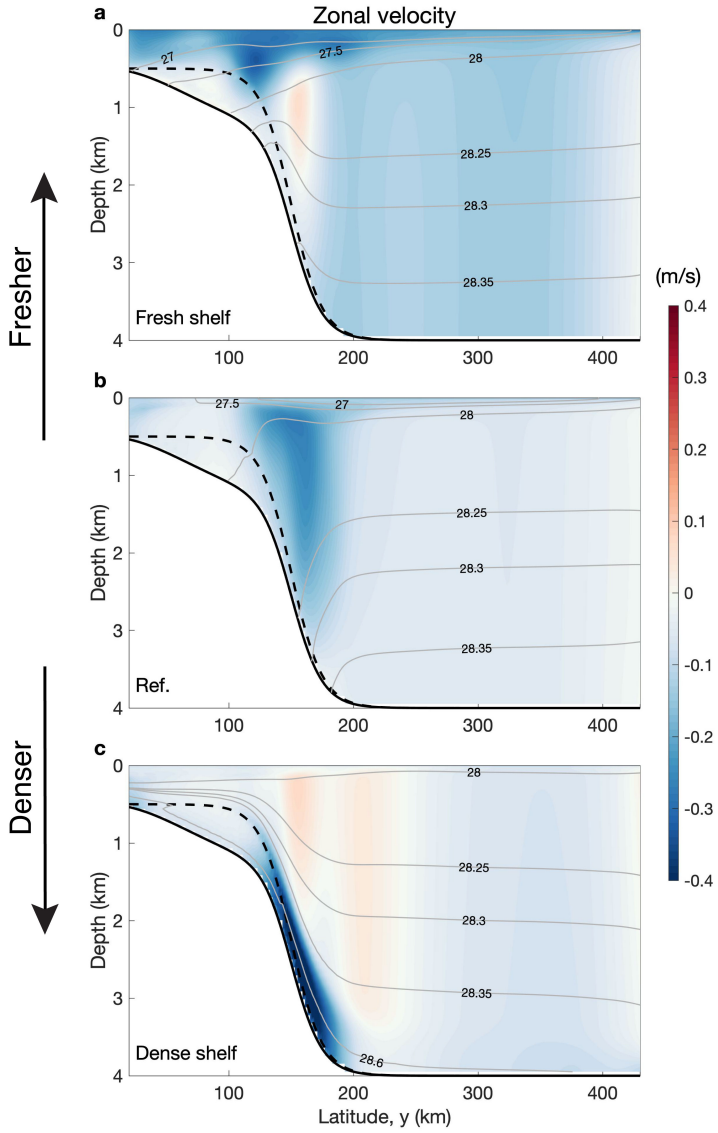

Extended Data Fig. 1 | **Time- and zonal-mean zonal (along-slope) circulation, overlaid by neutral density contours. a**, the fresh-shelf case. **b**, the reference case. **c**, the dense-shelf case. Blue denotes westward flow (into the page), and red denotes eastward flow (out of the page). The gray contours with numbers show the time- and zonal-mean neutral density (kg/m^3). The black solid and dashed curves denote the deepest and shallowest bathymetry, respectively. The 20-km sponge layers in the northern and southern boundaries are excluded.

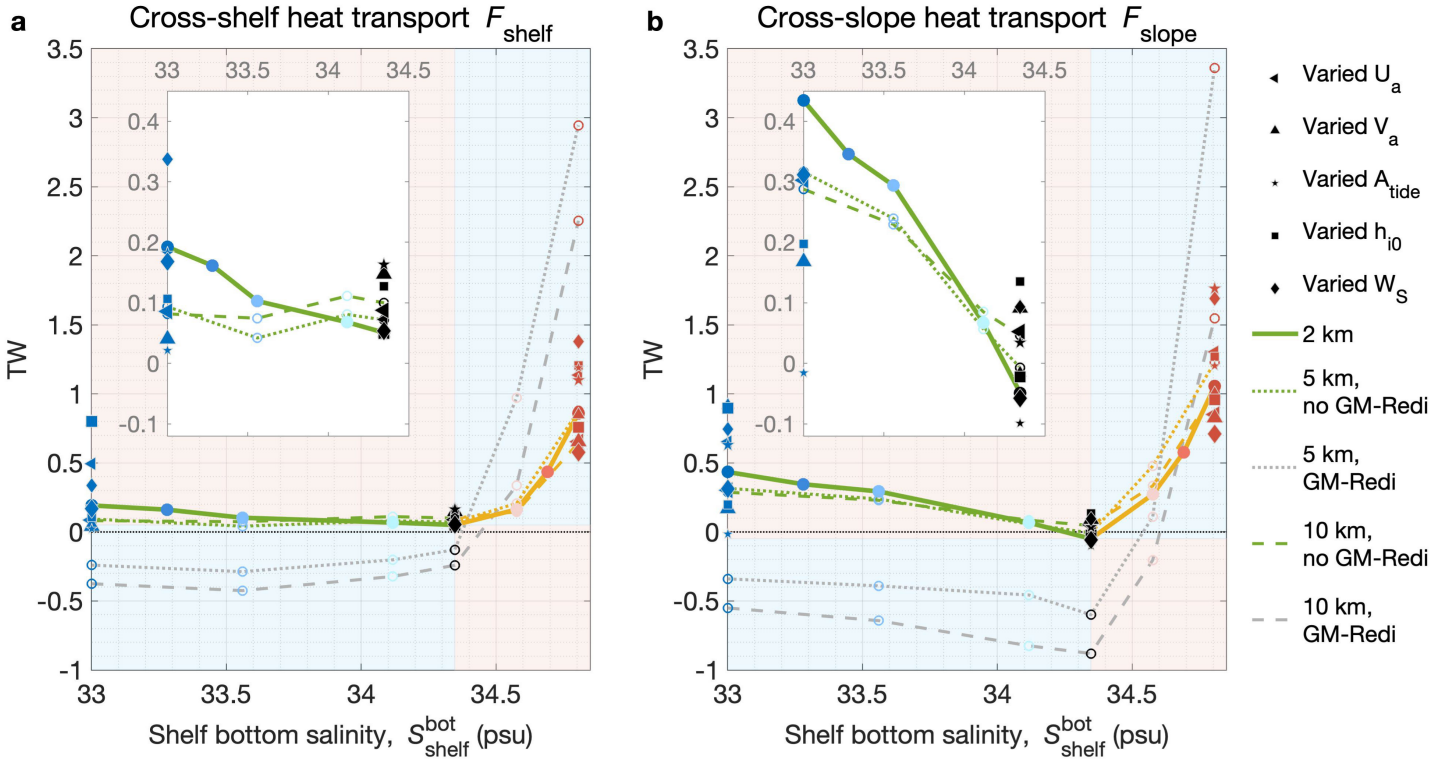

Extended Data Fig. 2 | Sensitivity of heat transferred onto the continental shelf (F_{shelf}) and to the upper part of the continental slope (F_{slope}). **a**, vertically and zonally integrated meridional advective heat flux averaged over the shelf region (y = 50 km–75 km), in unit TW (1 TW= 10^{12} W), as a function of shelf bottom salinity. The solid, dotted, and dashed lines denote simulations with 2-km, 5-km, and 10-km resolution, respectively. The colored and gray lines denote simulations with no GM-Redi eddy parameterization, and with GM-Redi, respectively. The insert is the zoom in of F_{shelf} in the fresh-shelf regime with the same axes. In the background, light red denotes regions of positive feedback, and light blue denotes regions of negative feedback. For the fresh-shelf, reference, and dense-shelf cases, the sensitivity of F_{shelf} to other model parameters are marked with various shapes, with larger marker sizes corresponding to larger values of the parameters. **b**, similar to panel **a**, but for the upper part of the continental slope (y = 125 km–150 km).

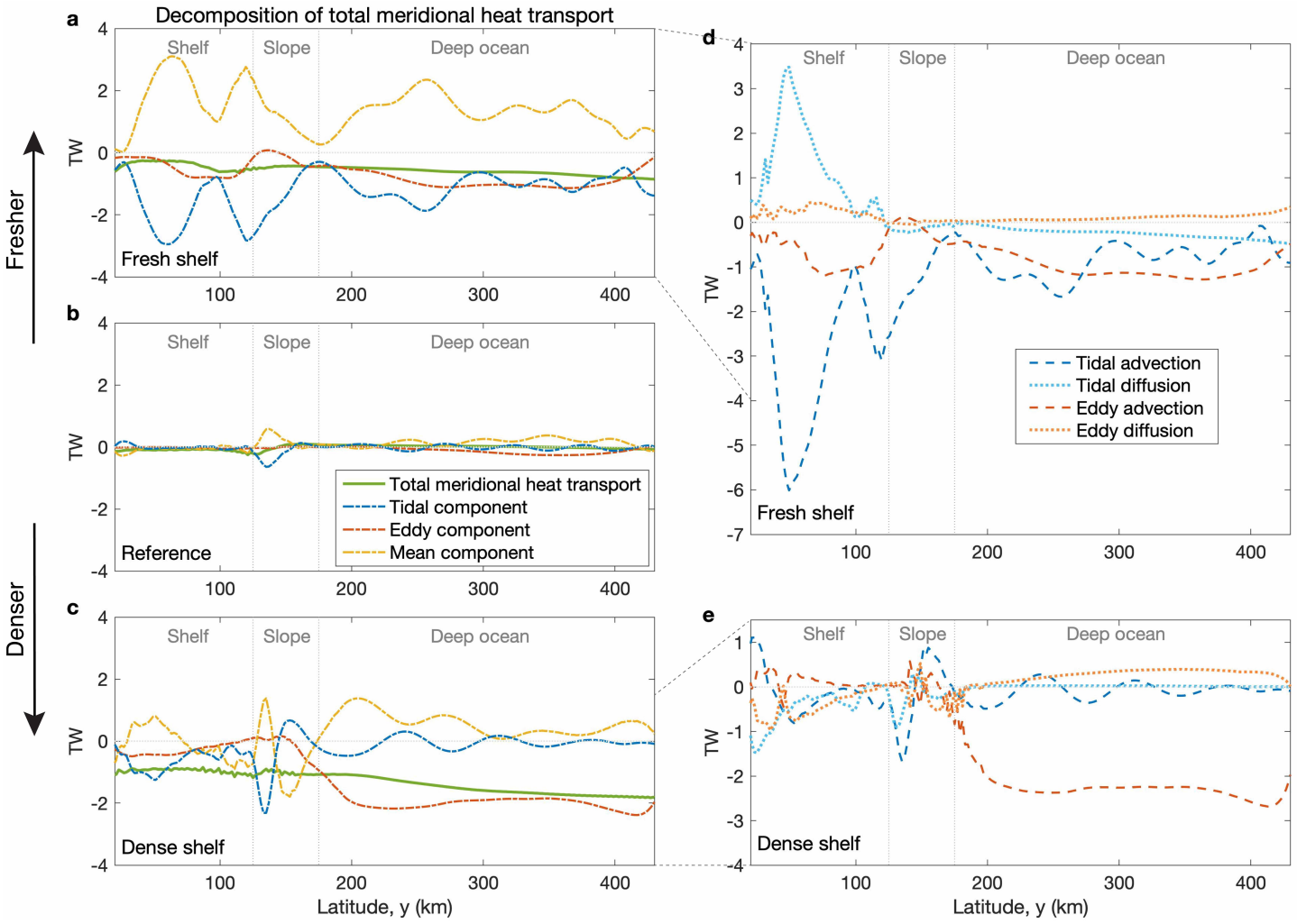

Extended Data Fig. 3 | Temporal decomposition of the total meridional heat transport. a-c, total meridional heat transport, and its tidal, eddy, and mean components in the fresh-shelf, reference, and dense-shelf cases. **d-e**, tidal advection, tidal diffusion, eddy advection, and eddy diffusion in the fresh-shelf and dense-shelf cases. In all panels, negative values correspond to shoreward (southward) heat transport. The 20-km sponge layers in the northern and southern boundaries are excluded.

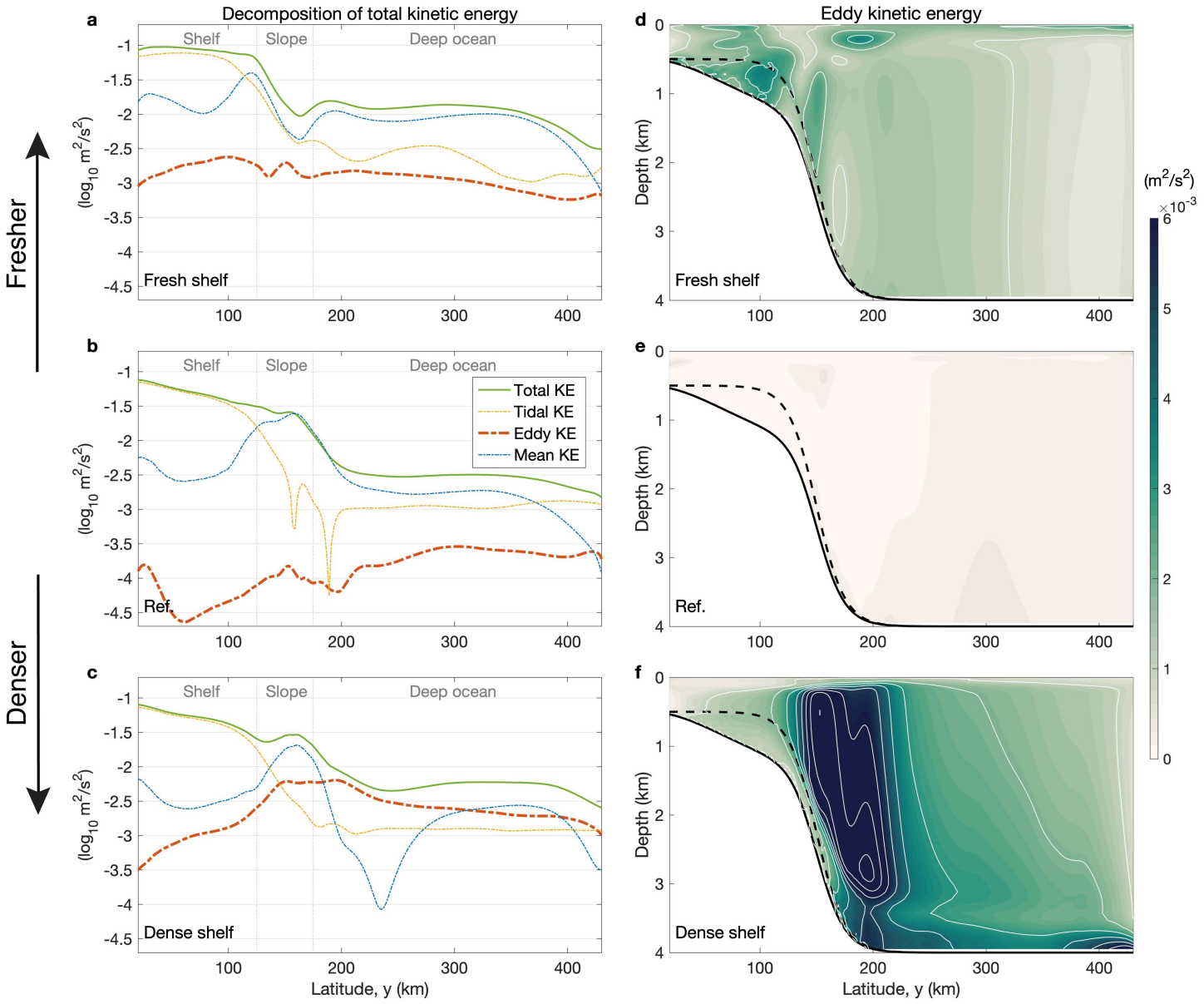

Extended Data Fig. 4 | **Temporal decomposition of the total kinetic energy. a-c**, time-, vertical- and zonal-mean total kinetic energy, and its tidal, eddy, and mean components in the fresh-shelf, reference, and dense-shelf cases. **d-f**, time- and zonal-mean eddy kinetic energy in the three cases. The colored and solid white contours show intervals of 1.5×10^{-4} m^2/s^2 and 10^{-3} m^2/s^2, respectively. The 20-km sponge layers in the northern and southern boundaries are excluded.

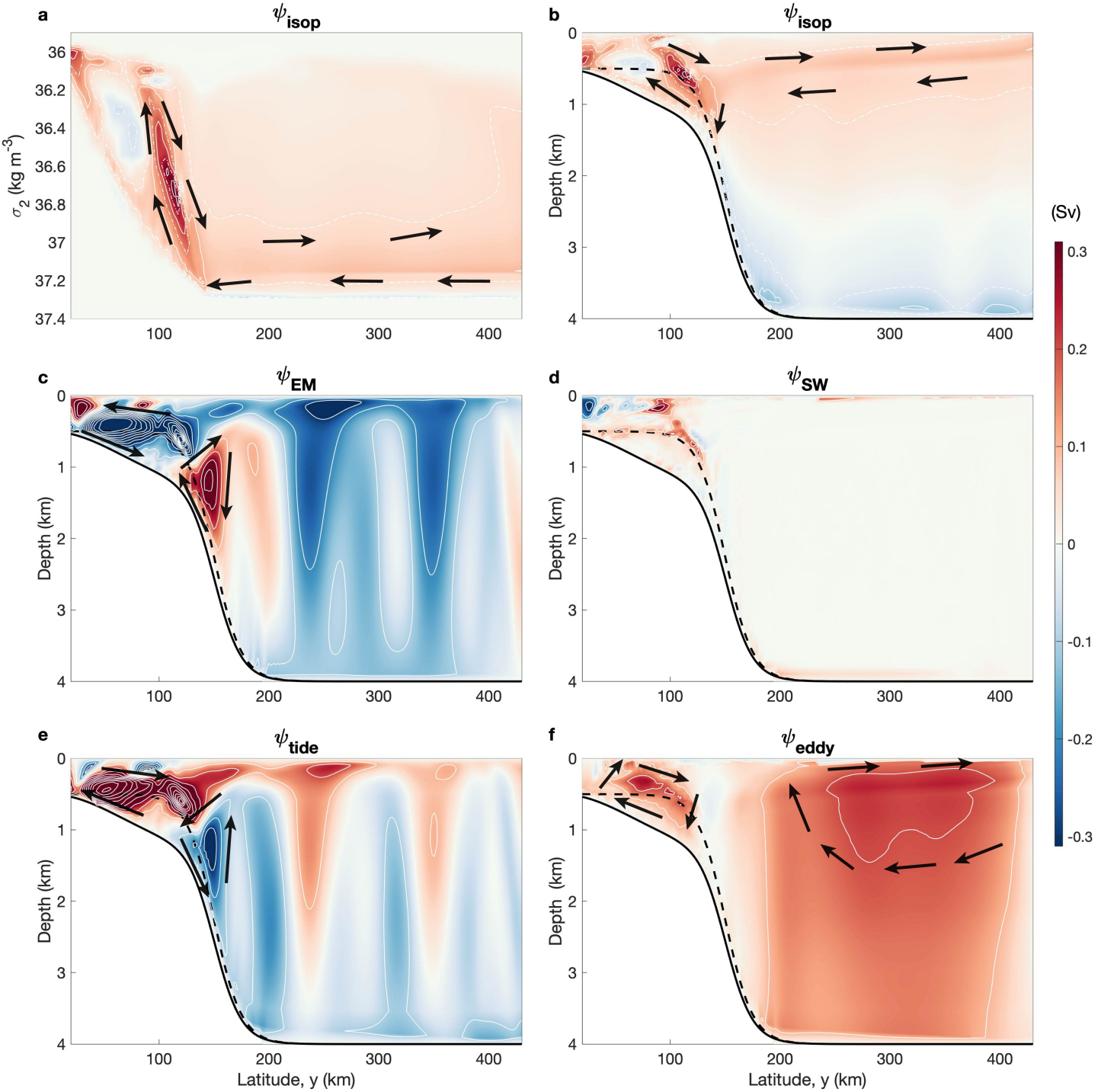

Extended Data Fig. 5 | **Temporal decomposition of the isopycnal overturning streamfunction ($\psi_{isop} = \psi_{EM} + \psi_{SW} + \psi_{tide} + \psi_{eddy}$) in the fresh-shelf case.** Isopycnal overturning streamfunction (ψ_{res}) with a reference depth of 2 km in potential density (σ_2) space (**a**) and z space (**b**). **c**, Eulerian-mean overturning streamfunction (ψ_{EM}). **d**, standing-wave overturning streamfunction (ψ_{SW}). **e**, tidal overturning streamfunction (ψ_{tide}). **f**, transient-eddy overturning streamfunction (ψ_{eddy}). The white dashed and solid contours show intervals of 0.05 Sv (1 Sv = 10^6 m^3/s) and 0.1 Sv, respectively. The black arrows show the direction of the overturning circulation, with positive values (red) corresponding to clockwise circulation, and negative values (blue) corresponding to counter-clockwise circulation. The black solid and dashed curves denote the deepest and shallowest bathymetry, respectively. The 20-km sponge layers in the northern and southern boundaries are excluded.

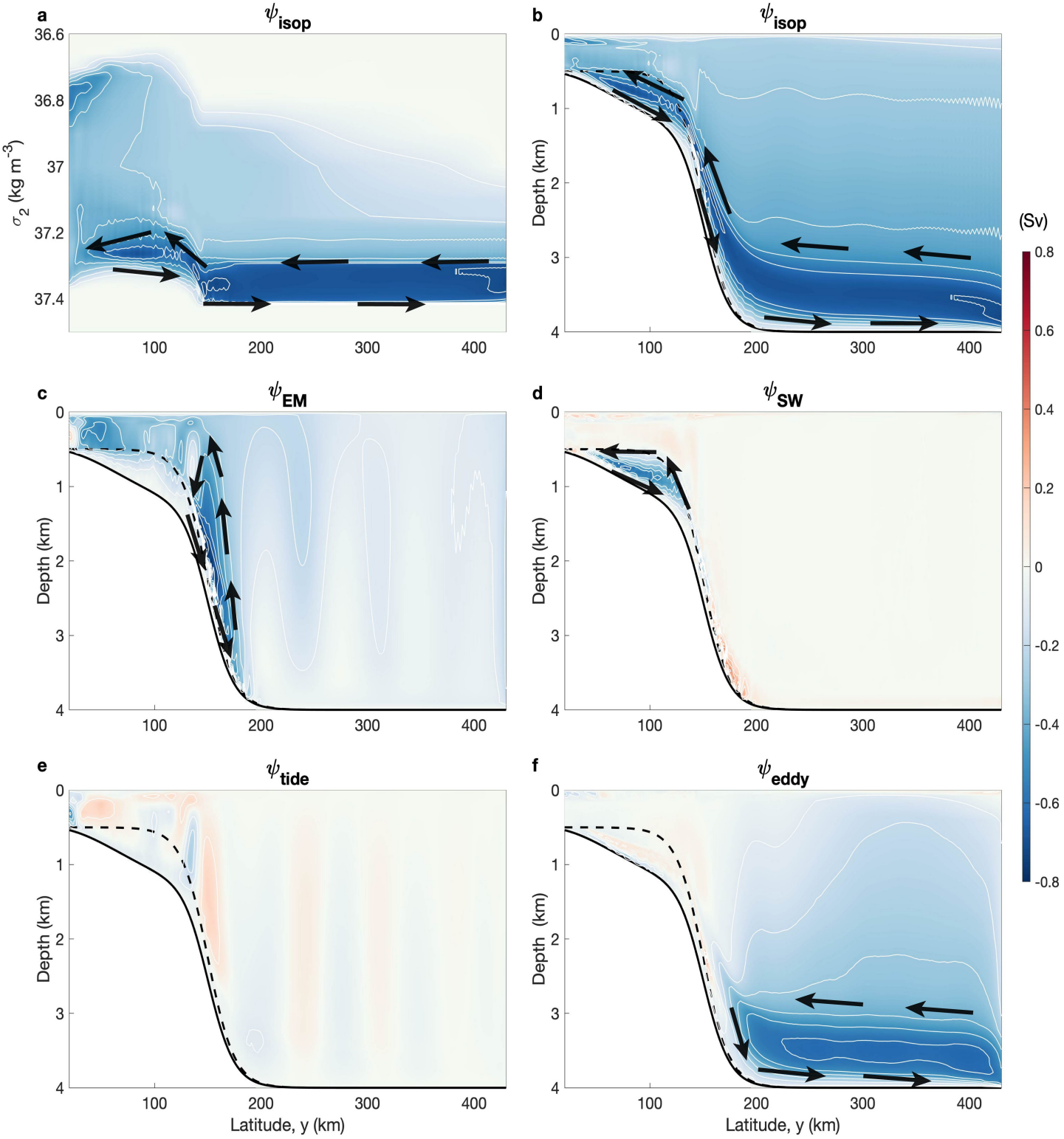

Extended Data Fig. 6 | Temporal decomposition of the isopycnal overturning streamfunction in the dense-shelf case. Similar to Extended Data Fig. 5, but for the dense-shelf case.